

Article

Calibration and Validation of Global Horizontal Irradiance Clear Sky Models against McClear Clear Sky Model in Morocco

Abderrahmane Mendyl^{1,*}, Brighton Mabasa², Houria Bouzghiba³ and Tamás Weidinger¹

¹ Department of Meteorology, Institute of Geography and Earth Sciences, ELTE Eötvös Loránd University, H-1117 Budapest, Hungary

² Research and Development Division, South African Weather Service, Pretoria 0001, South Africa

³ Doctoral School of Environmental Sciences, Hungarian University of Agriculture and Life Science, H-2100 Gödöllő, Hungary

* Correspondence: amendyl@student.elte.hu or mendyl.abderrahmane@gmail.com

Abstract: This study calibrated and compared the capabilities of hourly global horizontal irradiance (GHI) clear sky models for six Moroccan locations, using the McClear clear sky model as a reference. Complex clear sky models, namely Bird, Simplified Solis, Ineichen and Perez, and simple clear sky models, namely Adnot–Bourges–Campana–Gicquel (ABCG), Berger–Duffie, and Haurwitz were tested. The SOLCAST satellite-based dataset estimates were validated against the McClear clear sky model. pvlib python was used to configure the models, and ERA5 hourly fractional cloud cover was used to identify clear-sky days. The study period was from 2014 to 2021, and the study sites were in different climatic regions in Morocco. Bar graphs, tables, and quantitative statistical metrics, namely relative mean bias error (rMBE), relative root mean square error (rRMSE), relative mean absolute error (rMAE), and the coefficient of determination (R^2), were used to quantify the skill of the clear sky model at different sites. The overall rMBE was negative in 5/6 sites, indicating consistent overestimation of GHI, and positive in Tantan (14.4%), indicating frequent underestimation of GHI. The overall rRMSE varied from 6 to 22%, suggesting strong agreement between clear sky models and the McClear clear sky model. The overall correlation was greater than 0.96, indicating a very strong relationship. Overall, the Bird clear sky model proved to be the most feasible. Complex clear sky models outperformed simple clear sky models. The SOLCAST satellite-based dataset and ERA5 cloud fraction information could well be used with quantifiable certainty as an accurate clear sky model in the study region and in other areas where complex clear sky models' inputs are not available.

Keywords: clear sky model; global horizontal irradiance; calibration; validation; solar energy applications; pvlib python; SOLCAST; fifth-generation European Centre for Medium-Range Weather Forecasts atmospheric reanalysis (ERA5); statistical metrics



Citation: Mendyl, A.; Mabasa, B.; Bouzghiba, H.; Weidinger, T. Calibration and Validation of Global Horizontal Irradiance Clear Sky Models against McClear Clear Sky Model in Morocco. *Appl. Sci.* **2023**, *13*, 320. <https://doi.org/10.3390/app13010320>

Academic Editors: Harry D. Kambezidis and Basil Psiloglou

Received: 19 October 2022
Revised: 19 December 2022
Accepted: 22 December 2022
Published: 27 December 2022



Copyright: © 2022 by the authors. Licensee MDPI, Basel, Switzerland. This article is an open access article distributed under the terms and conditions of the Creative Commons Attribution (CC BY) license (<https://creativecommons.org/licenses/by/4.0/>).

1. Introduction

Morocco declared at the Conference of the Parties (COP21) of the United Nations Framework Convention on Climate Change (UN-FCCC) that it intends to increase its renewable energy capacity to 52% (20% solar, 20% wind, and 12% hydro) by 2030. Between 2018 and 2030, the country expects to install around 10 GW of renewable energy (RE) volume (4.5 GW of solar, 4.2 GW of wind, and 1.3 GW of hydroelectric) [1]. The purpose of this study is to calibrate and validate global horizontal irradiance (GHI) clear sky models in order to contribute to the establishment of a solar resource data bank and solar energy infrastructure in Morocco.

Clear sky models are used to estimate solar radiation under clear sky conditions, meaning when there are no visible clouds in the atmosphere, using solar geometry and other atmospheric parameters. Solar energy technologies for photovoltaic (PV) or thermal applications necessitate an evaluation of the available solar energy resource at the selected

location [2,3]. These measurements are frequently unavailable for the targeted areas and must therefore be estimated in clear sky conditions [4–7]. Even when in situ observations are available, there may be gaps in the observation records that must be filled in order to estimate the solar resource [8–10]. It is important to know how much solar energy is available at any given location, and clear sky irradiance, specifically GHI, provides that information. This information is essential for predicting or estimating the performance of solar energy technologies [11]. As a result, determining the clear sky GHI at a given location is important for projecting the optimum performance of solar technologies before they are implemented.

Various clear sky models with varying complexities of input meteorological factors have been developed and verified throughout time to estimate clear sky GHI for a variety of solar energy systems, particularly in areas where observations are unavailable. The clear sky models are either empirically based [12–14] or can be broadband [15,16]. Empirically based irradiance models need geometric parameters, such as solar zenith angle position, and/or key climatological parameters, such as sunshine duration, relative humidity, surface pressure, clearness of the atmosphere, and air temperature as input parameters [17,18], whereas broadband models need inputs that fully define the atmospheric state in detail, such as aerosol optical depth, amount of precipitable water, and ozone column [4,19–21]. Specific atmospheric or meteorological characteristics are not always available or are of low quality, limiting the model outputs' accuracy [21,22]. GHI at the ground surface can also be accurately estimated using satellite images [23–27].

The aim of this study is to determine the overall best model to estimate clear sky GHI in Morocco. The models Bird [13,28], Simplified Solis [29,30], Ineichen and Perez [31,32], Berger–Duffie [33], Adnot–Bourges–Campana–Gicquel (ABCG) [34], Haurwitz [35,36], and SOLCAST [37] were calibrated and validated against McClear clear sky model data [38]. The study's clear sky models were chosen based on the availability of input parameters. The models considered ranged from simple clear sky models (Berger–Duffie, ABCG, and Haurwitz) that require few input parameters (such as the sun's zenith angle (θ_z) and the top of the atmosphere's direct normal irradiance (DNI_{TOA})) to complex clear sky models (Ineichen and Perez, Bird, Simplified Solis) that require many input parameters in addition to θ_z and DNI_{TOA} , as summarized in Table 3. The SOLCAST satellite-based dataset was also included in the study because it performed best when validated against GHI observation data such as Mabasa et al. [39] in South Africa, Yang and Bright [40] globally using Baseline Surface Radiation Network (BSRN) [41] stations, and Bright [42] in all climatic regions. It was included in the study to investigate the possibility of using it with ERA5 hourly fractional cloud cover data [43] in estimating clear sky irradiance.

The McClear clear sky model was used as a reference because there were no observed GHI data to be used to validate the clear sky models in the study area. Among alternative data sets, the McClear clear sky model was chosen because it performed very well when compared to GHI observation data, for example [11,38,44,45], and it was already preconfigured. ERA5 hourly fractional cloud cover data [43] were used to identify clear-sky days in the study area because a recent study by Mabasa et al. [45] in South Africa confirmed that it can identify cloudy and clear-sky days. Comparing hourly model outputs to the McClear clear sky model outputs related to GHI would therefore establish the overall best method. To assess the capabilities of the clear sky models, quantitative statistical measures, namely relative mean bias error (rMBE), relative root mean square error (rRMSE), relative mean absolute error (rMAE), and the coefficient of determination (R^2) were used.

2. Literature Review

El Alani et al. [11] validated the McClear model [20] by comparing it to 1-min average GHI clear sky irradiance data in Benguerir (Green Energy Park, Morocco). The validation results are summarised in Table 1. The validation results showed that the McClear model can accurately estimate clear sky GHI in the context of Benguerir's unique environment, where skies are frequently clear. The validation results were used as a basis of forecasting

the 1-min GHI one day ahead. The study's challenge was not being able to do data quality control on observed GHI, which hindered the investigators from critically analysing the reasons for GHI overestimation. Laaroussi et al. [46] conducted a comparison study of observed and estimated GHI in Moroccan sites (Missour, Erfoud, Zagora, and Tantan). A comparison of the measured and estimated GHI revealed good agreement between them, and the results and quantifications are summarised in Table 1. However, these disparities were attributed to the consequence of the ground albedo, which was frequently present below the station's altitude due to the regular presence of clouds.

Gairaa et al. [47] evaluated the accuracy of five GHI clear sky models using 5-min interval data in Bourareah, Algeria and 10-min interval data in Ghardaia, the capital city of the Ghardaia Province in the northern-central region of Algeria in the Sahara Desert. The authors established that the European Solar Radiation Atlas (ESRA) [48,49] and Ineichen-Perez [31] models performed the best with results as summarised in Table 1. The authors recommended that the two models be used as a foundation for renewable energy applications in the study area.

Sun et al. [50] verified 75 GHI clear sky irradiance measurements, revealing that different clear sky models provided varying results in each climatic area. They also discovered that certain models performed inconsistently in various climates due to an overdependence on input, and that some model coefficients were created using datasets from climates that were completely different from the climates in other areas where the models were used. Laguarda and Abal [51] assessed the accuracy of the three clear sky models ESRA [48,49], Simplified Solis [29,30], and Kasten [52,53] by using data from five sites located in Uruguay and neighbouring countries (southeastern South America). The models chosen for evaluation were chosen based on the availability of relevant input data in the area. Clear sky conditions were automatically detected using Reno et al. [54]'s methodology. There was a negative MBE across all models and locations, indicating that GHI was underestimated and the rRMSE values were good, as shown in Table 1. Yang et al. [55] tested the accuracy of five clear sky models using one clear-sky day in Singapore. The models differed in performance, and the results were applied to build a new local model.

Ineichen [7] validated 8 clear sky GHI measurements across 20 sites using 16 independent input databases. The author found that Linke turbidity had the biggest influence on model dependability, and therefore that, rather than site-specific observed meteorological inputs, resulted in the models underestimating solar radiation. Gueymard et al. [56] and Badescu et al. [57] carried out tests to validate very simple clear sky and cloudy sky GHI models under the conditions of Romania's climate and geographical latitudes (Eastern Europe). In July, the MAE of the clear sky models ranged between 7 and 14%, and in January, it ranged between 12 and 19%.

Kwarikunda and Chiguvare [58] evaluated three distinct models that were tailored for the study area's geographical location and used to estimate clear sky GHI at three places in Namibia's subtropical desert climate (Kokerboom, Arandis, and Auas). The models were considered based on the availability of their input requirements. The validation results revealed that the models fit the observed data well; the validation results are summarized in Table 1. As a result, the modified models may be used to compute clear sky GHI in these study locations as well as other places with comparable climatic conditions. Between 2010 and 2013, Mghouchi et al. [59] evaluated the performance of three models for predicting GHI in Tetouan, northern Morocco: ASHRAE [60,61], the Campbell model [62], and the Benjamin model [63] which is also known as the Liu and Jordan model [64]. The authors observed that the ASHRAE model was more suited for estimating high-temporal resolution GHI, whereas the Campbell model was better suited for estimating monthly GHI at the study site.

Kallio and Riihelä [65] examined the estimated clear sky GHI in Finland using four models with different meteorological inputs. Aerosol Optical Depth and water vapour were the key meteorological inputs from the MACC and ERA-Interim reanalysis repositories, and almost all models underestimated GHI at the locations studied. McClear [38,44],

Ineichen [30,31], and Solis with default Pvlb inputs [30,66] all performed better. The inclusion of reanalysis inputs increased the Solis model's biases, which were caused by atmospheric optical depth (AOD) and water vapour climatology, both of which fail to accurately represent variability in specific locations and times.

Table 1. Overview of the verification results from the reviewed literature.

| Study | Year | Clear Sky Model | rMBE (%) | rRMSE (%) | R ² |
|-------------------------------|------|--|----------------------|--|------------------------------------|
| El Alani et al. [11] | 2021 | McClea | 0.6% | 2.2% | 0.96 |
| | | McClea (day ahead) | 0.8% | 3.3% | 0.99 |
| Badescu et al. [57] | 2013 | 54 models | - | 7–14%, | - |
| Laaroussi et al. [46] | 2016 | Various models | - | less than 30% | - |
| Gairaa et al. [47] | 2019 | European Solar Radiation Atlas (ESRA) | - | 6.26% | - |
| | | Ineichen–Perez | - | 3.84% | - |
| Sun et al. [50] | 2019 | 75 GHI clear sky irradiance models | - | - | - |
| Mghouchi et al. [59] | 2016 | ASHRAE [61,62], Campbell, [63] and Benjamin [64] | - | - | - |
| Laguarda and Abal [51] | 2017 | ESRA, Simplified Solis, and Kasten | Negative up to –5.3% | Range between 4.3% and 7% | - |
| Ineichen [7] | 2016 | Eight high clear sky solar irradiance models | Negative up to –1% | Range between 4% and 5% | - |
| Kwarikunda and Chiguvare [58] | 2021 | Berger–Duffie, Adnot–Bourger–Campana–Gicquel and Robledo–Soler | - | Range between 4% and 8% | Exceeded 0.98 for all three models |
| Pérez-Burgos et al. [5] | 2017 | Louche, Robledo–Soler, and European Solar Radiation Atlas | - | 9.9% to 5.7% 7.8% to 7.4% 8.8% to 6.7% 5.7% to 9.9% | - |
| Alam [67] | 2006 | REST, Yang, and CPCR2 | - | Up to 7%, 13.4%, and 25.9% | - |

Pérez-Burgos et al. [5] validated three GHI clear sky models adapted to the Madrid region. The validation was carried out by comparing the performance of the original and locally adapted models in estimating GHI; the results are summarized in Table 1. It was discovered that when the models were locally calibrated, there was a 4% improvement. They recommended that the study's calibration methodology be applied to areas with comparable climatic conditions. The study by Badescu et al. [57] examined fifty-four GHI clear-sky models, which is a significantly larger sample size than any previous work. The complexity of the models in the sample ranged from very simple to complex. Most of the models investigated have already been validated in various geographical areas at various periods and by using diverse validation methodologies. It is yet unknown how they correlate in a specific and uniform environment. The following limitations hindered the study: the input data required by the models did not correspond to what was available for the place and time, and the authors lacked the metadata that would have informed them about the accuracy of the data. As a result, missing data were generated by interpolation, extrapolation, or estimation, resulting in uncertainty in estimated GHI due to the inadequate information.

Gueymard's [4] study examined methods for identifying clear-sky times in the literature; the approach used a wide variety of inputs. Using data from a few days with varying cloudiness, the author found that various methods had advantages and disadvantages.

Bird and Hulstrom [13] investigated six GHI clear sky models using theoretical baseline dependence on transmittance, transmittance after molecular scattering, water vapor transmittance, and ozone transmittance. The study's findings contributed to the development of the Bird clear sky model. Gueymard [68] investigated the validity and effectiveness of 11 GHI clear sky models in estimating GHI. The representations of atmospheric effects in clear sky models were explored as well as their sensitivity to optical masses, Rayleigh scattering, ozone absorption, mixed gas absorption, water vapor absorption, and aerosol extinction. The models' accuracy was validated by comparing them to data obtained in situ at seven different locations in California, Canada, Belgium, Switzerland, France, and India. The more-physical models are found to be generally of higher accuracy and greater flexibility than empirical models.

Ineichen [69] evaluated 8 GHI clear sky models with 16 distinct databanks of observed GHI covering 20 years and stations, a range of altitudes including 1600 m, and a wide range of climates. Given the models' complexity, the author investigated the impact of atmospheric parameters and indicated that utilizing meteorological databanks rather than locally observed meteorological parameters resulted in underestimation of GHI by the models. According to the author, while accuracy is not heavily reliant on the model, model selection should be based on either the implementation convenience or the availability of input parameters. Younes and Muneer [70] analysed four GHI clear sky models at six different locations in the United Kingdom, Spain, and India. The Meteorological Radiation Model (MRM) performed best after being locally calibrated. REST2 [15] was the best performing model among uncalibrated models.

Gueymard [71] used atmospheric data to assess five models capable of forecasting DNI under clear skies. These models were tested against the results from 18 decomposition models that were used to predict DNI from GHI. The separation methods were found to be reasonable but not exceptionally accurate under clear conditions and significantly inaccurate under non-clear sky conditions. Gueymard [4] investigated 18 models for estimating GHI based on atmospheric data. Data from Oklahoma, Illinois, Colorado, Hawaii, and Saudi Arabia were compared to four simple and eight complex clear sky models. The study revealed that various models were capable of accurately estimating GHI. The REST2 model performed best, followed by the Ineichen model [69].

Alam [67] used hourly GHI from four Indian regions to analyze three GHI clear sky models. The REST model was found to be more accurate in Indian areas than the other two models, as indicated in Table 1. Using monthly average GHI data spanning 14 years, Ianetz et al. [72] investigated the comparative capabilities of four models for three locations in Israel's Negev region. To identify clear-sky days, Iqbal's [73] filter was used, which categorized days only based on their daily clearness index [72,73]. The authors discovered that the Berger–Duffie model, a model presented by Lingamgunta and Veziroglu [74], and a model proposed by Kondratyev [75] fared the best.

3. Description of the Clear Sky Models

In the Adnot–Bourges–Campana–Gicquel (ABCG) model [34], the sun's zenith angle (θ_z) (for different methods for calculation, see [76–78] for examples) is the main input that is required to be able to estimate clear sky GHI. The transmittance of 951.39 is already calibrated. The attenuation of extraterrestrial normal incoming irradiance (DNI_{TOA}) as it passes through the atmosphere is affected by the θ_z . The Bird, Ineichen and Perez, Simplified Solis, McClear, Berger–Duffie, and Haurwitz clear models were elucidated in the study by Mabasa et al. [45]. The SOLCAST satellite-based dataset was also elucidated in [39,40,42]. The basic models' equations are given by Equations (1)–(7).

Adnot–Bourges–Campana–Gicquel [34]:

$$GHI = 951.39 \cdot \cos \theta_z^{1.15} \quad (1)$$

Bird [13]:

$$GHI = \frac{(DNI \cos \theta_z + DIF)}{(1 - R_g R_s)} \quad (2)$$

Ineichen and Perez [32]:

$$GHI = 0.84 DNI_{TOA} \cos \theta_z e^{(-0.027 AM (f_{h1} + f_{h2} (T_L - 1)))} \quad (3)$$

Simplified Solis [30]:

$$GHI = DNI'_{TOA} e^{\left(\frac{-\tau_g}{\cos \theta_z^2}\right)} \cdot \cos \theta_z \quad (4)$$

In Equation (4), to account for varying altitudes and atmospheric conditions, the DNI_{TOA} was changed to the enhanced direct normal extraterrestrial solar radiation DNI'_{TOA} , given by the equation below from Ineichen [30]:

$$DNI'_{TOA} = DNI_{TOA} \left(0.12 P_w^{0.56} \cdot AOD_{700nm}^2 + 0.97 P_w^{0.032} \cdot AOD_{700nm} + 1.08 P_w^{0.0051} + 0.017 \ln\left(\frac{p}{1013}\right) \right) \quad (5)$$

Be Berger–Duffie [33]:

$$GHI = DNI_{TOA} 0.7 \cos \theta_z \quad (6)$$

Haurwitz [35]:

$$GHI = 1098 \cos \theta_z e^{\frac{-0.057}{\cos \theta_z}} \quad (7)$$

The variables in Equations (1)–(7), can be defined as follows: DNI is the direct normal extraterrestrial irradiance; DIF is the diffuse horizontal irradiance; R_g is the ground albedo; R_s is the sky albedo; DNI_{TOA} is the direct normal extraterrestrial irradiance; AM is the relative air mass; f_{h1} and f_{h2} are the coefficients that relate the site altitude with the altitude of the atmospheric interactions; T_L is the atmospheric transmissivity; τ is the total atmospheric optical depth; b is the constant of adjustment for DNI; P_w is the precipitable water or water vapour in centimetres and AOD_{nm} is the aerosol optical depth at 700 nanometres and p is the surface pressure.

4. Materials and Methods

4.1. Study Area

The study sites were in Morocco, a country in North Africa. Tantan, Fes, Agadir, Marrakech, Ouarzazate, and Tangier were the study sites, as shown in Figure 1 and Table 2. The country has a population of 37 million people and a land area of 710,850 square kilometers. According to the climate change knowledge site [79], northern and southern Morocco have highly diverse climates. The Atlantic Ocean, Mediterranean Sea, and Sahara Desert all have a significant influence on rainfall and temperature. The rainiest months are October through May. High temperatures prevail in the southern and southeastern dry and semi-arid regions, with average monthly temperatures ranging from 9.4 °C (December, January) to 26 °C in Morocco (July, August). The months with the most rain are October to April, and the months with the least rain are June to August [79]. The Moroccan Agency for Energy Efficiency (AMEE) and the National Center of Meteorology recently collaborated to create a new climatic zoning map for Morocco [80,81]. All of the new climate zones in Morocco share similar solar irradiation, altitude, and other key climatic characteristics. A key city serves as the indicator for each zone, as shown in Figure 1.

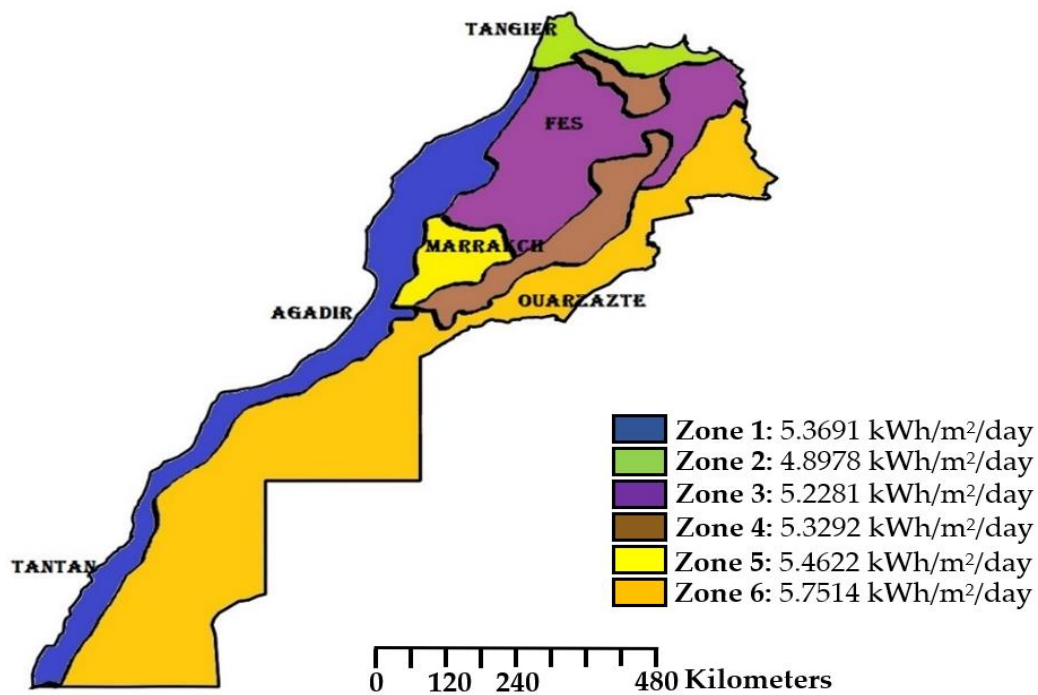


Figure 1. A map showing the climatic zones and solar intensities of the study sites. The map was sourced from: www.marocmeteo.ma (accessed on 16 March 2022) [81].

Table 2. A table showing study area: Latitude, longitude, altitude, climate region or climate type, mean annual values of relative humidity, water vapour, the total number of clear-sky days used per site where the percentage of the annual average share of clear-sky days is given in brackets.

| Station | WMO Code | Latitude (° N) | Longitude (° E) | Altitude (m) | Köppen Climate Type | Number of Clear-Sky Days | Relative Humidity (%) | Water Vapor (g/kg) |
|------------|----------|----------------|-----------------|--------------|---|--------------------------|-----------------------|--------------------|
| Marrakech | 60230 | 31.617 | −8.033 | 466 | Mid-Latitude Steppe and Desert Climate (Bsh). | 196 (24.5%) | 55 | 0.16 |
| Fes | 60141 | 33.933 | −4.983 | 579 | Mediterranean Climate (Csa) | 138 (17.25%) | 38 | 0.11 |
| Agadir | 60252 | 30.383 | −9.567 | 23 | Mid-Latitude Steppe and Desert Climate (Bsh) | 130 (16.25%) | 61 | 0.17 |
| Tangier | 60100 | 35.733 | −5.803 | 21 | Mediterranean Climate (Csa) | 38 (4.75%) | 73 | 0.19 |
| Ouarzazate | 60262 | 30.933 | −6.910 | 1140 | Tropical and Subtropical Desert Climate (Bwh) | 232 (29%) | 59 | 0.16 |
| Tantan | 60285 | 28.437 | −11.103 | 45 | Tropical and Subtropical Desert Climate (Bwh) | 62 (7.75%) | 64 | 0.18 |

4.2. Data and Methodology

As shown in Table 3, different clear sky models necessitate different sets of input parameters. There are a few input parameters that apply to all different models.

Table 3. A table summarising different inputs required by different models.

| Input/Model | Bird | Simple Solis | Ineichen–Perez | McClear | Haurwitz | Berger–Duffie | ABCG |
|--------------------|------|--------------|----------------|---------|----------|---------------|------|
| Zenith Angle | X | X | X | X | X | X | X |
| Albedo | X | - | - | X | - | - | - |
| AOD1240 nm | X | X | - | - | - | - | - |
| AOD550 nm | X | X | - | X | - | - | - |
| AOD380 nm | X | - | - | - | - | - | - |
| AOD500 nm | X | - | - | - | - | - | - |
| AOD700 nm | - | X | - | - | - | - | - |
| Temperature | X | X | - | X | - | - | - |
| Humidity | X | X | - | X | - | - | - |
| $DN I_{TOA}$ | X | X | X | X | - | X | X |
| D (Julian day) | X | X | X | X | X | X | X |
| Solar constant | X | X | X | X | - | - | - |
| Pressure | X | X | X | X | - | - | - |
| Altitude | X | X | X | X | X | X | X |
| Linke Turbidity | - | - | X | - | - | - | - |
| Ozone | X | - | - | X | - | - | - |
| Absolute airmass | - | - | X | - | - | - | - |
| Relative airmass | X | - | X | - | - | - | - |
| Apparent Elevation | - | X | - | - | - | - | - |
| Asymmetry | X | - | - | - | - | - | - |
| Total inputs | 16 | 12 | 9 | 11 | 3 | 4 | 4 |

4.2.1. Meteorological Data (Temperature, Humidity, Pressure)

Temperature, humidity, and pressure data were sourced from Meteomanz [82]. Meteomanz delivers observed meteorological data from global sites sourced from surface synoptic observations (SYNOP) and Binary Universal Form for the Representation of meteorological data (BUFR) information supplied by accredited meteorological stations as well as forecast atmospheric information derived from Global Forecast System (GFS) models and European Centre for Medium-Range Weather Forecasts (ECMWF). The data were accessible as 3-h averages; the linear interpolation method was used to obtain hourly averages from the 3-h averages.

Observation data were sourced for the eight-year period of 2014–2021. Quality control of raw datasets was provided based on the semiempirical method [83]. Missing data were filled in. Minor data gaps (up to six measurement cycles missing) were filled in using the linear regression method; for longer data gaps, gap-filling was performed using data from the preceding method and 1–3 days prior to the data gap, leaving a maximum of three hours of adjustment time to fit the measured and interpolated data. It is noted that the distribution of the SYNOP stations and quality of observations in Morocco are better than in most other parts of Africa [84,85]. Water vapour was calculated from hourly temperature and hourly humidity data using a methodology given by [45,86–89]. The methodology used is summarised by Equations (8) to (12):

$$P_w = 0.1 \cdot H_V \cdot P_V \quad (8)$$

where H_V is the apparent water vapor scale height (in km) and P_V is the surface water vapor density (in $\frac{g}{m^3}$). These are given by Equations (9) and (11), respectively:

$$H_V = 0.4976 + 1.5265 \cdot X + e^{(13.68 \cdot X - 14.9188 \cdot X^3)} \quad (9)$$

$$\text{With } X = \frac{T}{273.15} \quad (10)$$

$$P_V = 216.7 \cdot RH \cdot \frac{e_s}{T} \quad (11)$$

$$\text{With } e_s = e^{(22.33 - \frac{4914}{T} - \frac{109220}{T^2} - 0.0039015 \cdot T)} \quad (12)$$

where T is the temperature (in °C) and RH is the relative humidity (in %).

4.2.2. Ozone Data

Ozone (O_3) is an oxygen molecule composed of three oxygen atoms. Its role in the atmosphere is to act as a sunscreen, i.e., it shields the Earth against dangerous ultraviolet (UV) rays from the Sun. O_3 in the atmosphere is a powerful absorbent of solar energy that enters the atmosphere. It is a greenhouse gas. At wavelengths less than 295–300 nm, no irradiance reaches the Earth's surface. The amount of O_3 in the atmosphere affects the Earth's surface radiation at a wavelength between 300 and 315 nm. The O_3 data used in the study were sourced from CAMS [90,91] as monthly climatological averages, with monthly O_3 climatological average values representing all the O_3 hourly values for that month.

4.2.3. Linke Turbidity Data

The Linke turbidity factor (TL, for an air mass of 2) is a good way to determine how the sun's rays are absorbed and scattered by the atmosphere under clear skies. When the sky is clear, TL can be used to determine how much solar radiation is attenuated by the atmosphere. If the atmosphere is clear and dry, then the TL would be equal to 1. The depletion of solar radiation by the clear-sky environment affects the value of TL. The TL data used in the study were sourced from CAMS [91] as monthly climatological means, with monthly TL climatological average values representing all the TL hourly values for that month.

4.2.4. Aerosol Optical Depth

The aerosol optical depth (AOD) is the coefficient of irradiance attenuation by the atmosphere. AOD data used in the study were sourced from SODA [92] as 3-h averages. AOD 1240 nm, AOD 550 nm, AOD 500 nm, AOD 380 nm, and AOD 700 nm were calculated using the Angstrom law [93,94]. The Angstrom law methodology was also applied by [45,86] in their clear sky model studies. The Angstrom turbidity law [93,94] was applied as follows: the Angstrom exponent (α) of the aerosol from the two known AOD wavelengths was found, and then the calculated α from those two known wavelengths was used to calculate the unknown AO. Equations (13) to (18) from [93,94] were used for this:

$$\frac{\tau_\lambda}{\tau_{\lambda_0}} = \left(\frac{\lambda}{\lambda_0} \right)^{-\alpha} \quad (13)$$

$$\tau_\lambda = \tau_{\lambda_0} \left(\frac{\lambda}{\lambda_0} \right)^{-\alpha} \quad (14)$$

$$\tau_{700nm} = \tau_{\lambda_0} \left(\frac{700 \text{ nm}}{\lambda_0} \right)^{-\alpha} \quad (15)$$

$$\tau_{500nm} = \tau_{\lambda_0} \left(\frac{500 \text{ nm}}{\lambda_0} \right)^{-\alpha} \quad (16)$$

$$\tau_{380nm} = \tau_{\lambda_0} \left(\frac{380 \text{ nm}}{\lambda_0} \right)^{-\alpha} \tag{17}$$

where:

- τ_{λ} is the optical thickness at unknown wavelength (AOD_{380} , AOD_{500} and AOD_{700});
- τ_{λ_0} is the optical thickness at the known wavelength (AOD_{550} or AOD_{1240});
- λ is the wavelength of the unknown AOD (AOD_{380} , AOD_{500} and AOD_{700});
- λ_0 is the wavelength of the known AOD (AOD_{550} or AOD_{1240});
- α is the angstrom, or alpha exponent, of the aerosol. It is related to the particle size distribution.

The alpha exponent, or Angstrom, of the aerosol (α) is calculated as in Equation (18):

$$\alpha = -\log \left[\frac{\left(\frac{\tau_{\lambda_1}}{\tau_{\lambda_2}} \right)}{\left(\frac{\lambda_1}{\lambda_2} \right)} \right] \tag{18}$$

where $\frac{\tau_{\lambda_1}}{\tau_{\lambda_2}}$ is the ratio of known optical thickness measurements $\frac{AOD_{550}}{AOD_{1240}}$ and $\frac{\lambda_1}{\lambda_2}$ is the ratio between the known wavelengths $\frac{550nm}{1240nm}$.

4.2.5. Albedo Data

Albedo is a measure of a surface’s ability to reflect sunlight. Light-coloured surfaces (high albedo) return a notable amount of the sun’s energy back into the atmosphere. Dim surfaces (low albedo) absorb large amounts of the sun’s light. Surface albedo is a way to measure how much short-wave irradiance is reflected away from the Earth’s surface. The albedo data used in the study were sourced from EUMETSAT’s Satellite Application Facility on Climate Monitoring (CMSAF) [95] as pentads. The desert has a high albedo, but because of its relatively dry and cloud-free atmosphere, its hot surface emits a lot of infrared radiation into space.

4.2.6. Solar Geometry

The solar angles were calculated with pvlib python using the Solar Position Algorithm (SPA) [66,96]. The solar zenith angle θ_z is given in Equation (19) and in [73,97] as:

$$\cos \theta_z = \sin \varnothing \cdot \sin \delta + \cos \varnothing \cdot \cos \delta \cdot \cos \omega \tag{19}$$

where \varnothing is the altitude of the site and δ is the solar declination angle in terms of the day of the year (D) as given by Cooper [98] and shown as Equation (20):

$$\delta = \text{solar declination} = -23.45 \sin \left(\frac{360(D + 284)}{365} \right) \tag{20}$$

where ω is the hour angle, given by [66,98,99] and as shown in Equation (21):

$$\omega = 15^\circ \cdot (ST - 12) \tag{21}$$

and with:

$$ST = STD + 4 \cdot (L_{st} - L_{local}) + E \tag{22}$$

where ST is solar time, STD is local standard time, L_{st} is the standard meridian for the local time zone, L_{local} is the local longitude, and E is the equation of time given by Equation (23).

$$E = 229.18(0.000075 + 0.001868 \cos B - 0.032077 \sin B - 0.014615 \cos 2B - 0.04089 \sin 2B) \tag{23}$$

$$B = (D - 1) \cdot \frac{360}{365} \tag{24}$$

Duffie and Beckman [97] defined the relative air mass (AM), which is the optical path length where irradiance is scattered and absorbed when the sun is not directly overhead, as Equation (25):

$$AM = \frac{1}{\cos \theta_z} \tag{25}$$

Kasten and Young [100] proposed that the relative air mass model given by Equation (25) should be modified to account for the curvature of the Earth. Equation (26) gives the modified version, which is the formulation used in this study:

$$AM = \frac{1}{\cos \theta_z + 0.50572 \cdot (6.07995 + (90 - \theta_z))^{-1.6364}} \tag{26}$$

To account for the effects of altitude, multiply the relative air mass by station pressure (in pascals) divided by pressure at sea level (101325). According to Bird et al. [101], this pressure-corrected air mass is known as absolute air mass (AM_a), which is given in Equation (27):

$$AM_a = p \cdot \frac{AM}{101325} \tag{27}$$

where p is the station pressure in pascals.

4.2.7. Extraterrestrial Solar Irradiance

The amount of solar radiation arriving at the top of the Earth’s atmosphere is approximated by extraterrestrial solar irradiance. Direct normal extraterrestrial irradiance (DNI_{TOA}), is the irradiance that is perpendicular to the direction of solar radiation and is given by Equation (28) as in Duffie and Beckman [97]:

$$DNI_{TOA} = \left(\frac{r}{R^2}\right) I_{SC} \tag{28}$$

where $I_{SC} = 1367 \frac{W}{m^2}$, the solar constant recommended by the World Meteorological Organization recommendation, according to Gueymard [102];

r is the middle distance of Earth from the Sun;

R is the instantaneous distance of the Earth from the Sun;

the ratio $\left(\frac{r}{R^2}\right)$ is the eccentricity factor, E_o , which by approximation is:

$$E_o = 1 + 0.0333 \cos \left[\left(\frac{2\pi D}{365} \right) \right] \tag{29}$$

where D is the Julian day. Thus, Equation (29) is approximated as:

$$DNI_{TOA} = \left[1 + 0.0333 \cos \left(\frac{2\pi D}{365} \right) \right] \cdot I_{SC} \tag{30}$$

4.3. Methodology

Figure 2 summarizes the methodology used in the study. The process began with the collection of ERA5 hourly fractional cloud cover data [43], i.e., the average portion of the sky covered by clouds when observed from a specific location per each study station from 2014 to 2021. The hourly data were summed to produce daily fractional cloud cover data for each site. A clear-sky day occurred when the daily fractional cloud cover for each station was zero. Following the identification of clear-sky days, the hourly McClear clear sky model data timesteps were compared to modelled clear-sky data. Each model’s clear-sky data were generated by solving the algorithms in Section 3 and entering parameters in Table 3. The matched timesteps of data were further filtered by considering only the hours when the zenith angle was less than 90 degrees, i.e., only the hours between sunrise and sunset, during the validation process. Each model’s performance was benchmarked using statistical metrics.

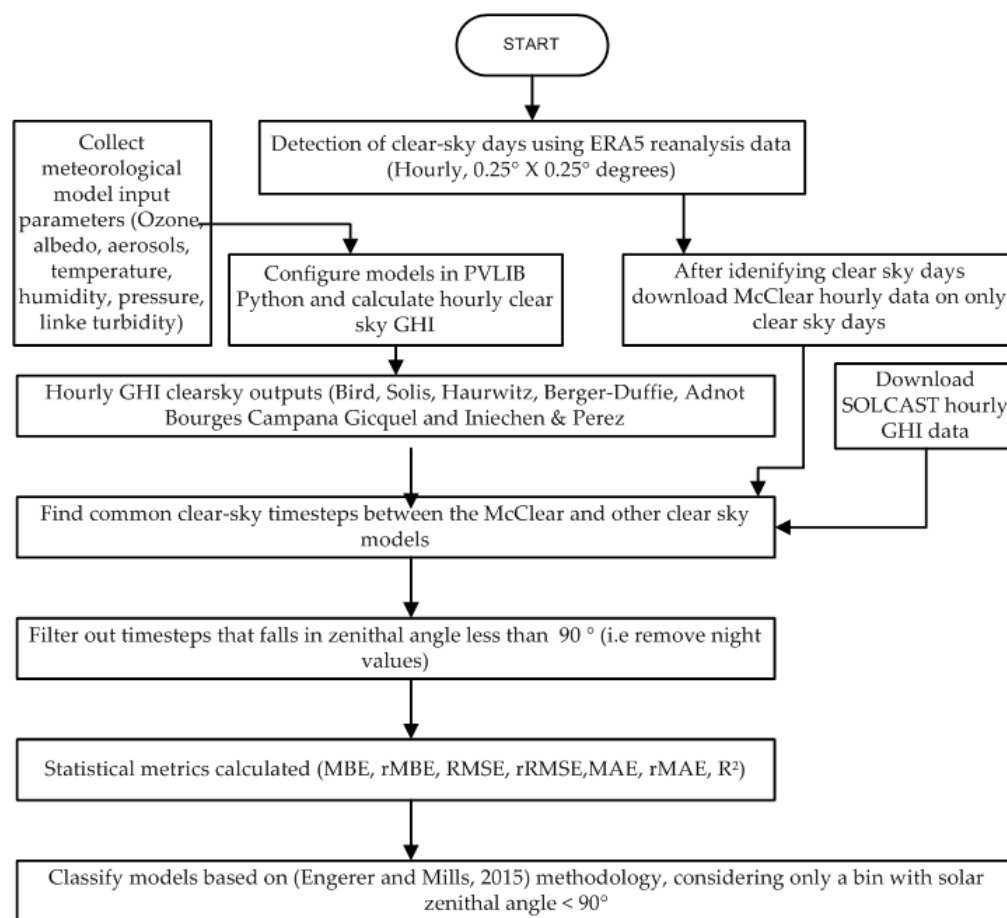


Figure 2. The schematic outline of the procedure used from model input data collection to clear sky detection, model configuration, and model data validation.

Table 4. Four performance classes to rank clear sky GHI models.

| Model Skill | rMBE | rRMSE | R ² |
|-------------|-------------------|------------|----------------|
| Poor | ≥ ±10 % | ≥15% | ≤0.97 |
| Average | ≥ ±5 %, < ±10 % | ≥10%, <15% | >0.97, ≤0.98, |
| Good | ≥ ±2 %, < ±5 % | ≥5%, <10% | >0.98, ≤0.99, |
| Excellent | < ±2 % | <5% | >0.99 |

4.4. Model Validation Using Statistical Metrics

The statistical metrics that were used to quantify the performance of the clear sky models are described here, one of which is the relative mean bias error (rMBE), which reflects the degree of error in percentage terms. A higher rMBE means that the model performed poorly, and a lower rMBE means that the model performed excellently. When the rMBE value is negative, it implies that the model overestimates GHI, while positive rMBE values imply that the model underestimates GHI. The relative root mean square error (rRMSE) is another percentage error measure that measures the degree of error in percentage terms. The rRMSE is not affected by the direction of the error, and it places additional emphasis on big errors. A greater rRMSE value means that the model performed poorly, while a smaller rRMSE value means that the model performed very well. The relative mean absolute error (rMAE), which quantifies the definite value of the error between the measured and estimated values, was also considered in the study as it gives a better outlook of estimation skill. A higher value of rMAE implies that the model has low estimation skill, while a low rMAE implies that the model has higher estimation skill and accuracy. The coefficient of determination (R^2) is a quantitative gauge of the extent of the

correlation between the change of the estimated and measured variables in a certain period. The nearer R^2 is to 1, the more suitable the accuracy of the prediction. The equations of the metrics are given in Equations (31) to (37) below.

$$MBE = \frac{1}{n} \sum_{i=1}^n (P_i - O_i) \quad (31)$$

$$rMBE = 100 * \frac{1}{n} \sum_{i=1}^n (P_i - O_i) \quad (32)$$

$$MAE = \frac{1}{n} \sum_{i=1}^n |P_i - O_i| \quad (33)$$

$$rMAE = 100 * \frac{1}{n} \sum_{i=1}^n \frac{|P_i - O_i|}{\bar{O}_i} \quad (34)$$

$$RMSE = \sqrt{\frac{1}{n-1} \sum_{i=1}^n (P_i - P_o)^2} \quad (35)$$

$$rRMSE = \frac{100}{\bar{O}_i} * \sqrt{\frac{1}{n-1} \sum_{i=1}^n (P_i - P_o)^2} \quad (36)$$

$$R^2 = 1 - \frac{\sum_{i=1}^n (P_i - O_i)^2}{\sum_{i=1}^n (P_i - \bar{O}_i)^2} \quad (37)$$

where O_i is the measured value, P_i is the predicted value, \bar{O}_i is the mean of the measured values, P_o is the observed value, i is the time point, and n is the total number of points used.

4.5. Model Benchmark

Each model's performance was evaluated using a classification methodology developed by Engerer et al. [103]. The classification limits for a model's skill are summarised in Table 4. The colouration in the table aids in identifying a model's skill in addition to quantitative margins, with blue depicting excellent skill, green depicting good skill, yellow depicting average performance, and pink depicting poor performance. The table was adapted from [101] and was previously applied by [45,104].

4.6. Most Feasible Clear Sky Model per Station

The most feasible model at each of the 6 sites was decided by initially selecting the best performing models for each metric. Then, from that group, the most feasible model at a site was the model with the maximum count across all statistical metrics. A quantitative comparison of the most favourable barometer was computed as the maximum tally of the four statistical metrics (rMBE, rRMSE, rMAE, and R^2).

5. Results

5.1. SOLCAST Results

SOLCAST overestimated GHI (i.e., negative rMBE) at Agadir (−5%), Ouarzazate (−13%), Tangier (−3%), and Marrakech (−4%), as shown in Figure 3. However, at the Fes station, rMBE was 0%, indicating that the estimates from GHI SOLCAST and McClear were comparable. The Tantan station (+21%) had an underestimation of GHI (i.e., positive rMBE). Figure 4 shows that the hourly rRMSE was less than 10% at four stations: Marrakech (5%), Tangier (4%), Fes (9%), and Agadir (8%), indicating a low bias between the datasets. This indicates very good agreement between McClear and SOLCAST at the Marrakech and Tangier stations, and good agreement (based on Table 4 model benchmarks) at the Fes and Agadir stations. The rRMSE was greater than 20% at Ouarzazate (20%) and Tantan (27%),

indicating high bias between the datasets and poor agreement between SOLCAST and McClear at these two locations.

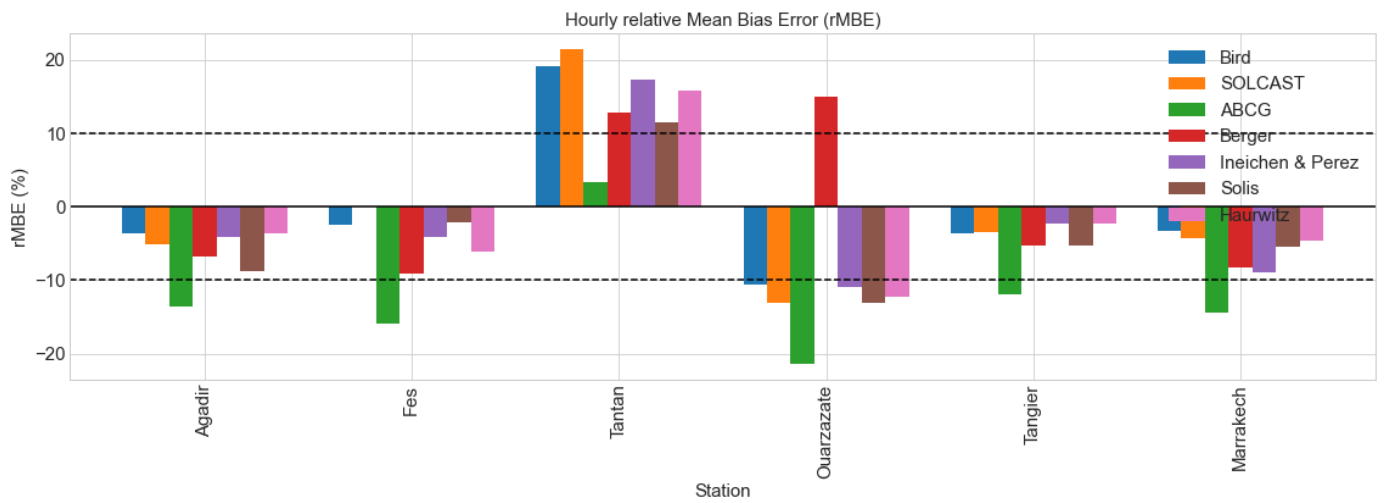


Figure 3. Hourly relative mean bias error (rMBE) of modelled clear sky GHI against McClear clear sky GHI.

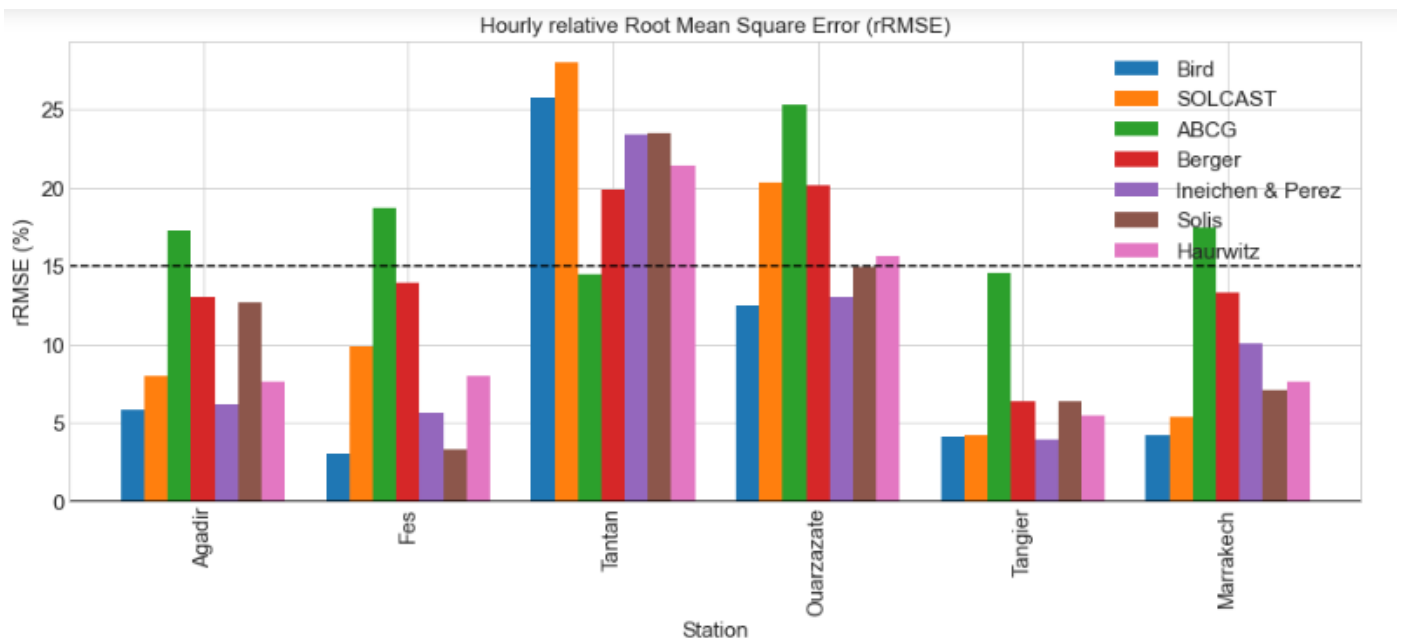


Figure 4. Hourly relative root mean square error (rRMSE) of modelled clear sky GHI against McClear clear sky GHI.

Figure 5 shows that three stations, Marrakech (5%), Tangier (3%), and Agadir (5%), had rMAEs less than 5%, indicating low bias between the datasets and very good agreement between McClear and SOLCAST at these three locations. In Fes and Ouarzazate, there was good agreement, with rMAEs less than 10% and 15%, respectively, whereas Tantan (23%) had poor agreement as indicated by high bias.

Table 5, which indicates the coefficient of determination (R^2) at all six stations, shows that $R^2 > 0.99$ in three stations, namely Agadir (0.995), Marrakech (0.999), and Tangier (0.999), indicating excellent performance based on Table 4 model benchmarks. At the Fes station, the coefficient was (0.985), indicating good correlation between SOLCAST and the McClear clear sky model. At Ouarzazate (0.96) and Tantan (<0.97), the correlation was less than 0.97; this shows poor correlation between SOLCAST and the McClear clear sky

model. In Figure 6, SOLCAST was closer to McClear, indicating good agreement but with variations between stations. The performance of SOLCAST model with stations is also summarised in the supplementary material Tables S1 to S6 and Figure S6.

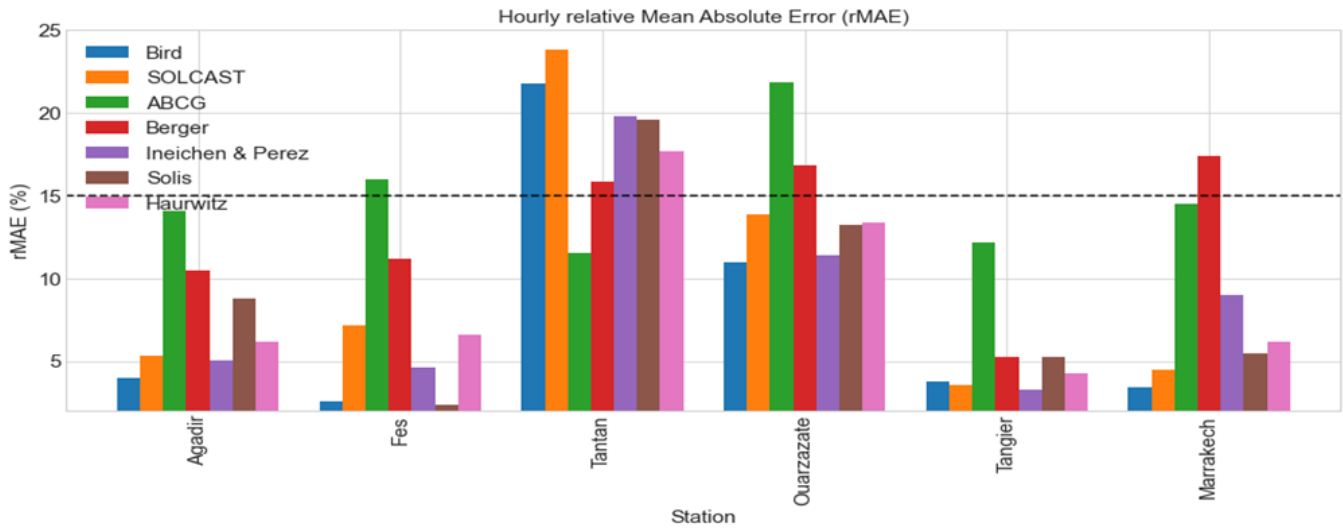


Figure 5. Hourly relative mean absolute error (rMAE) of modelled clear sky GHI against McClear clear sky GHI.

Table 5. Hourly mean observed GHI (W/m^2) and coefficient of determination (R^2) of clear sky models against GHI measured in situ.

| Station | Mean GHI (W/m^2) | Solis | SOLCAST | Bird | Haurwitz | Ineichen and Perez | ABCG | Berger |
|------------|----------------------|-------|---------|-------|----------|--------------------|-------|--------|
| Marrakech | 518.1 | 0.997 | 0.999 | 0.998 | 0.99 | 0.998 | 0.99 | 0.99 |
| Fes | 494.7 | 0.999 | 0.985 | 0.999 | 0.997 | 0.998 | 0.996 | 0.996 |
| Agadir | 485.9 | 0.988 | 0.995 | 0.997 | 0.99 | 0.997 | 0.99 | 0.99 |
| Tangier | 545.2 | 0.998 | 0.999 | 0.999 | 0.996 | 0.998 | 0.996 | 0.998 |
| Ouarzazate | 518.3 | 0.99 | 0.96 | 0.99 | 0.99 | 0.99 | 0.98 | 0.99 |
| Tantan | 379.5 | 0.95 | 0.97 | 0.97 | 0.98 | 0.97 | 0.98 | 0.97 |

5.2. Bird Results

According to Figure 3, the GHI was overestimated at Agadir (−3.5%), Ouarzazate (−10.5%), Tangier (−3.7%), and Marrakech (−3.2%), but it was underestimated at Tantan (19.2%). According to Figure 4, rRMSE was less than 10% at four stations, namely Agadir (5.9%), Fes (3.0%), Tangier (4.2%), and Marrakech (4.2%), indicating low bias between McClear and Bird. The rRMSE at the Tantan station was greater than 25%, indicating poor agreement between McClear and Bird at this station. Figure 5 shows that four stations, namely Agadir (4%), Fes (2.6%), Tangier (3.8%), and Marrakech (3.4%), had rMAEs less than 5%, indicating low bias between the datasets and very good agreement between the McClear and Bird models at these four locations. While rMAE was less than 15% in Ouarzazate (11.0%), indicating average performance, rRMSE was (21.8%), indicating poor agreement as indicated by high bias. Table 5 shows the coefficient of determination (R^2) at each of the six stations, with $R^2 > 0.99$ in all cases, indicating excellent performance based on Table 4, with the exception of Tantan whose coefficient was (0.96), indicating a poor relationship between the Bird and McClear models. The performance of Bird clear sky model with stations is also summarised in the supplementary material Tables S1 to S6 and Figure S1.

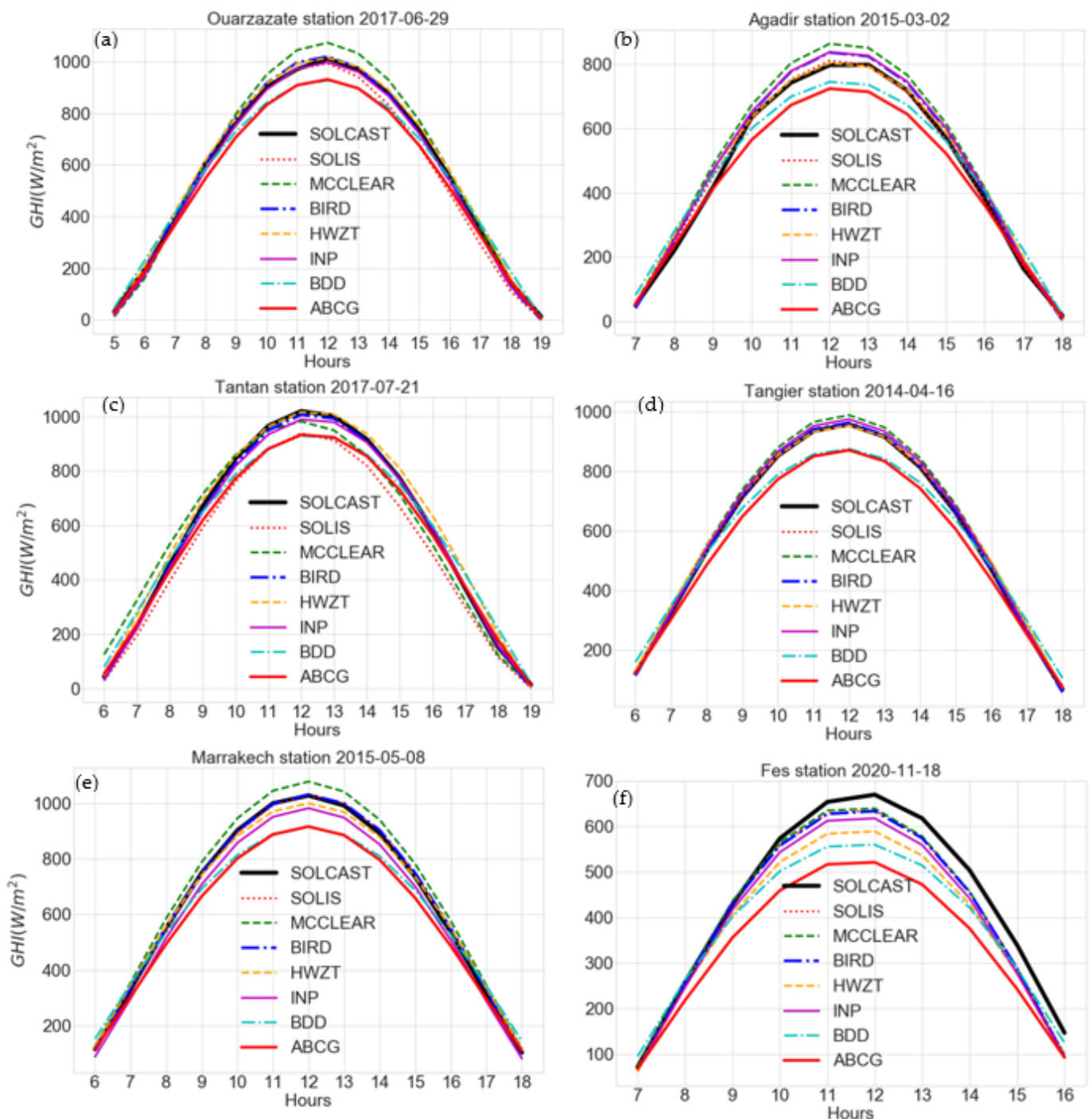


Figure 6. Comparison between McClear and modelled clear sky hourly GHI values in Ouarzazate (a), Agadir (b), Tantan (c), Tangier (d), Marrakech (e), and Fes (f).

5.3. Adnot–Bourges–Campana–Gicquel (ABCG) Results

From Figure 3, ABCG overestimated the GHI at Marrakech (−14.5%), Tangier (−11.9%), Ouarzazate (−21.4%), Agadir (−13.5%), and Fes (−15.9%), whereas it was underestimated at Tantan (3.4%). From Figure 4, which gives the hourly rRMSE, rRMSE was less than 15% in Tantan (14.5%) and Tangier (14.6%), which shows average agreement in these stations between McClear and ABCG, whereas it was more than 15% in the other stations, which indicates poor agreement in these stations between McClear and ABCG. From Figure 5, which indicates rMAE, at four stations, namely Agadir (14.1%), Tantan (11.6%), Tangier (12.2%), and Marrakech (14.7), the rMAEs were less than 15%, which shows good agree-

ment. However, at Ouarzazate (21.9%) and Fes (16.0%), the rMAEs were greater than 15%, indicating poor agreement as indicated by high bias.

From Table 5, which indicates the coefficient of determination (R^2) at all six stations, $R^2 > 0.99$ in all stations, indicating excellent performance based on Table 4 with the exception of Ouarzazate with good performance (0.98) and Tantan (<0.98), where the coefficient of (0.97) indicates poor correlation between the ABCG and McClear clear sky models based on Table 4 model benchmarks. From Table 6, ABCG was feasible at one station: Tantan. Here, it had a minimum rMBE and maximum R^2 of (0.99). According to Figure 6, the ABCG clear sky model was not closer to McClear, showing poor agreement but differing at various stations. The performance of ABCG clear sky model with stations is also summarised in the supplementary material Tables S1 to S6 and Figure S2.

Table 6. Best-performing clear sky models per hourly statistical metrics, most feasible model, and rank of performance (classification).

| Station | Minimum rMBE | Minimum rRMSE | Minimum rMAE | Maximum R^2 | Most Feasible | Rating |
|------------|--------------|---------------|--------------|----------------|---------------|---------------|
| Marrakech | BIRD | BIRD | BIRD | BIRD/SOLCAST | BIRD | 4/4 |
| Fes | SOLCAST | BIRD | Solis | Bird/SOLIS/IPN | Solis | 2/4 |
| Agadir | HWZT | BIRD | BIRD | BIRD/IPN | BIRD | $\frac{3}{4}$ |
| Tangier | IPN | IPN | IPN | BIRD/SOLCAST | IPN | $\frac{3}{4}$ |
| Ouarzazate | BIRD | BIRD | BIRD | SOLIS/IPN | BIRD | $\frac{3}{4}$ |
| Tantan | ABCG | ABCG | ABCG | ABCG | ABCG | 4/4 |

5.4. Berger–Duffie (BDD) Results

From Figure 3, BDD overestimated GHI in four stations, namely Marrakech (−8.2%), Tangier (−5.2%), Fes (−9.1%), and Agadir (−6.8%), whereas it underestimated GHI at Ouarzazate (14.9%) and Tantan (12.9%). From Figure 4, which gives the hourly rRMSE, rRMSE was less than 15% in Agadir (13.1%), Tangier (6.3%), and Marrakech (13.4%), which shows average agreement at these station between McClear and BDD. rRMSE was more than 15% at the rest of the stations, which indicates poor agreement between McClear and BDD. From Figure 5, which indicates rMAE, two stations, Agadir (10.5%) and Fes (11.2%), had rMAEs of less than 15% and thus showed good agreement, while poor agreement was shown at the rest of the stations with rMAE of greater than 15%, indicated by high bias.

From Table 5, which indicates the coefficient of determination (R^2), $R^2 > 0.99$ in all stations indicating excellent performance with the exception of Ouarzazate, showing good performance (<0.99), and the Tantan (0.97) station, where the coefficient indicates poor correlation between BDD and McClear clear sky model based on Table 4 model benchmarks. From Table 5, BDD was not feasible at any of the six stations based on Section 4.6 criteria when compared to other clear sky models. From Figure 6, BDD was not closer to McClear, which shows poor agreement that varies at different stations. The performance of BDD clear sky model with stations is also summarised in the supplementary material Tables S1 to S6 and Figure S3.

5.5. Ineichen and Perez (INP) Results

From Figure 3, INP overestimated GHI in five stations, namely Marrakech (−9.0%), Tangier (−2.2%), Ouarzazate (−10.9%), Fes (−4.2%), and Agadir (−4.2%), whereas it was underestimated at Tantan (17.3%). From Figure 4, which gives the hourly rRMSE, rRMSE was less than 15% in Agadir (13.1%), Tangier (6.3%), Marrakech (13.4%), and Fes (13.9%), which shows average agreement at these stations and between McClear and SOLCAST,

whereas it was more than 15% at the Tantan (20.0%) and Ouarzazate (20.1%) stations, which indicates poor agreement in these stations between McClear and SOLCAST. From Figure 5, which indicates rMAE, all stations' rMAE values were less than 15%, which shows good agreement with the exception of the Tantan (19.8%) station, where rMAE was greater than 15%, thus indicating poor agreement as indicated by high bias.

From Table 5, which indicates the coefficient of determination (R^2) at all six stations, $R^2 > 0.99$ in all stations, indicating excellent performance based on Table 4 except the Tanat (0.97) station, where the coefficient indicates poor correlation between the INP and McClear clear sky models. From Table 6, INP was feasible at Tangier station, showing minimum rMBE at Tangier and maximum R^2 of (0.99) at Ouarzazate, Agadir, and Fes. From Figure 6, INP was closer to McClear, which shows good agreement that varies at different stations. The performance of INP clear sky model with stations is also summarised in the supplementary material Tables S1 to S6 and Figure S5.

5.6. Simplified Solis Results

From Figure 3, Simplified Solis overestimated GHI in five stations, namely Marrakech (−5.4%), Tangier (−5.2%), Ouarzazate (−13.0), Fes (−2.1%), and Agadir (−8.7%), whereas it underestimated GHI at Tantan (11.5%). From Figure 4, which gives the hourly rRMSE, rRMSE was less than 15% at Agadir (12.7%), Tangier (4.2%), Marrakech (4.2%), and Fes (3.0%), which shows average agreement in this station and between the McClear and Simplified Solis clear sky model, while it was more than 15% at Tantan (25.7%) station which indicate poor agreement in this station and between McClear and Simplified Solis clear sky model.

From Figure 5, which indicates rMAE, all of the stations showed an rMAE of less than 15%, which shows good agreement, except for the Tantan (19.6%) station where rMAE was greater than 15%, thus indicating poor agreement as indicated by high bias. From Table 5, which indicates the coefficient of determination (R^2) at six stations, all stations showed $R^2 > 0.99$, indicating excellent performance based on Table 4 with the exceptions of the Agadir (<0.99) station, where the coefficient indicates average correlation, and Tantan (0.95), where the coefficient indicates poor performance. From Table 6, Solis was feasible at Fes station, and it has a maximum R^2 of (0.99) at Fes and Ouarzazate. From Figure 6, Solis was closer to McClear, which shows good agreement that varies at different stations. The performance of Solis clear sky model with stations is also summarised in the supplementary material Tables S1 to S6 and Figure S7.

5.7. Haurwitz Results

From Figure 3, the Haurwitz clear sky model overestimated GHI in five stations, namely Marrakech (−4.6%), Tangier (−2.3%), Ouarzazate (−12.2%), Fes (−6.1%), and Agadir (−3.5%), whereas it underestimated GHI at Tantan (15.9%). From Figure 4, which gives the hourly rRMSE, rRMSE was less than 15% in Agadir (7.7%), Tangier (5.4%), Marrakech (7.7%), and Fes (8.0%), showing average agreement in these stations between the McClear and Haurwitz clear sky models. It was more than 15% at the Tantan (21.4%) and Ouarzazate (15.7%) stations, which indicates poor agreement in these stations. From Figure 5, which indicates rMAE, all of the stations showed an rMAE of less than 15%, which shows good agreement, with the exception of the Tantan (17.7%) station where rMAE was greater than 15%, thus indicating poor agreement as indicated by high bias.

From Table 5, which indicates the coefficient of determination (R^2) at all six stations, $R^2 > 0.99$ in all stations, indicating excellent performance based on Table 4, with the exception of the Ouarzazate (<0.99) station, where the coefficient indicates average correlation, and Tantan (0.97), where the coefficient indicates poor correlation between the Haurwitz and McClear clear sky models. From Table 6, Haurwitz was not feasible at any of the six stations based on Section 4.6. criteria when compared to other clear sky models, and it has the minimum rMBE at Agadir. From Figure 6, Haurwitz was closer to McClear, which shows good agreement that varies at different stations. The performance of Haurwitz clear

sky model with stations is also summarised in the supplementary material Tables S1 to S6 and Figure S4.

6. Discussions

According to Table 2, Table 6, and Figures 3–5, there was no significant variation in model performance between sites with different humidity content, number of clear-sky days per year, and annual water vapour content. However, there was a notable variation when considering Tantan, the station with the lowest latitude 28.437 (° N), and Tangier, the station with the highest latitude 35.733 (° N). The differences were as follows: from Figure 3, when comparing these two sites with extreme latitudes, all the clear sky models underestimated GHI at the Tangier station as shown by negative rMBE values, and it is also noted that small values of rMBE less than -10% were reported with the exception of the ABCG model (-11.9%). At the Tantan station, except for the ABCG model (3.4%), positive large rMBE values greater than $+10\%$ were observed. This means that the ABCG model, a simple clear sky model that only depends on the sun's zenith angle, performed well at low-latitude sites, while the other models considered in the study performed well at high-latitude sites. Farahat et al. [105] also discovered a substantial fluctuation in solar radiation with latitude in Saudi Arabia, and after dividing the study region $\{15\text{--}55\text{ (°S)}\}$ into 5° intervals, they reported the best tilt angles to be 20 (° S) , 25 (° S) , and 30 (° S) , depending on the location.

When comparing rMAE and rRMSE at these two sites, the Tantan station performed poorly, with both rMAE and rRMSE values greater than 10% in all models except for ABCG, whereas the Tangier station performed well, with both rMAE and rRMSE values less than 10% in all models except for ABCG.

When considering coefficient of determination (R^2), all clear sky models at Tangier had R^2 greater than 0.988 , whereas all clear sky models at Tantan had R^2 less than 0.977 . This demonstrates that latitude affects the performance of clear sky models, with high latitude favouring the ABCG clear sky model and low latitude favouring complex models. It was also observed that, overall, complex models outperformed simple clear sky models.

The SOLCAST satellite-based dataset had a comparable performance with complex clear sky models, and it performed better than simple clear sky models except in two locations with extreme altitudes, Tantan (45 m) and Ouarzazate (1140 m), where it showed poor performance, indicating that SOLCAST performs poorly at both very high and very low altitudes. Overall, SOLCAST and ERA5 cloud cover can be used together as an accurate clear sky model in areas where complex clear sky models do not have inputs.

McClear is not a perfect model and may introduce some bias that affects validation results in some areas, even though its inputs are high resolution and it has demonstrated excellent performance in various studies around the world. Another study limitation was the lack of reference observation GHI data to validate the clear sky models. Using reference data, future studies will validate models, particularly McClear. Another limitation was the lack of hourly aerosol data, so 3-h aerosols from CAMS AOD had to be interpolated. AOD 380 nm , 700 nm , and 500 nm were unavailable, and the AOD at 1240 nm had to be derived and interpolated; this could have influenced the results.

Even though [27,101] discovered that ozone does not vary much over time and has a low influence on GHI, using monthly averages may introduce some bias. High spatial and temporal resolution model inputs are necessary to fully assess the performance of the clear sky model. To solve this challenge, meteorological institutions collecting observations should also record these critical meteorological parameters (albedo, ozone, water vapour, Linke turbidity, cloud cover, and aerosols).

7. Conclusions

The study validated and evaluated the performance of clear sky models, namely Bird, Simplified SOLIS, Ineichen and Perez, including simple clear sky models Adnot-Bourges-Campana-Gicquel (ABCG), Berger-Duffie, and Haurwitz as well as the SOLCAST

satellite-based dataset against the McClear clear sky model (see also Equations (1)–(7)). The study period ranged from 2014 to 2021 at five sites with different climates, namely Marrakech, Agadir, Fes, Tangier, and Ouarzazate.

ERA5 was used to filter out cloudy days. ERA5 and SOLCAST satellite-based data sets can be used as a clear sky model tool in the study area and in regions where there are no inputs to calibrate complex clear sky models.

The models were configured using pvlib python, and different input parameters were gathered per the requirements of each model, ranging from those of simple models, which require simple input parameters, to those of complex models, which require more input parameters. Statistical metrics have been calculated, namely the relative mean bias error (rMBE), the relative root mean square error (rRMSE), the relative mean absolute error (rMAE), and the coefficient of determination (R^2). The models were ranked according to how well they performed in the study area.

The Bird clear sky model was the overall most feasible model in the study area. ABCG showed overall poor performance, but it was the best performer at Tantan station, a site with low latitude 28.437 ($^{\circ}$ N). The SOLCAST satellite-based dataset performed better than simple clear sky models, but it struggled in very low (45 m) and very high (1140 m) altitude sites. In the absence of meteorological inputs to calibrate complex clear sky models, SOLCAST and ERA5 cloud data can be used to filter clear-sky days.

The availability of observation data, particularly GHI data measured in situ, was a challenge in this study; as a result, the McClear clear sky model was used as a reference.

Supplementary Materials: The following supporting information can be downloaded at <https://www.mdpi.com/article/10.3390/app13010320/s1>. Table S1–Table S6, which show clear sky model-estimated GHI versus McClear model prediction at all six stations studied with validation statistical metrics. The colours in the tables are used to indicate the clear sky model's skill in estimating GHI-based statistical metrics, with blue representing excellent performance, green representing good performance, yellow representing average performance, and pink representing poor performance. Figure S1–Figure S7 show the scatter plots of McClear-modelled hourly GHI against other clear sky model-modelled hourly GHI at all six stations under study.

Author Contributions: Conceptualization, A.M. and T.W.; methodology, A.M. and B.M.; software, A.M. and B.M.; validation, A.M. and T.W.; formal analysis, A.M. and T.W.; investigation, A.M. and H.B.; resources, A.M.; writing—original draft preparation, A.M.; writing—review and editing, H.B. and T.W.; visualization, A.M. and B.M.; supervision, T.W.; project administration, A.M. and T.W. All authors have read and agreed to the published version of the manuscript.

Funding: This research was funded by National Research, Development, and Innovation Office Fund grant number K138176. This research is also supported by the Stipendium Hungaricum Doctoral Scholarship of the Tempus Public Foundation where the first author is the beneficiary.

Institutional Review Board Statement: Not applicable.

Informed Consent Statement: Not applicable.

Data Availability Statement: Not applicable.

Acknowledgments: The authors thank the Copernicus Atmosphere Monitoring Service (CAMS) Solar Radiation Data (SoDa) for providing freely available Linke turbidity data, ozone data, aerosol optical depth data, and McClear model data on their website; the European Centre for Medium-Range Weather Forecasts (ECMWF) for providing freely available ERA5 hourly cloud data on their website; the European Organization for the Exploitation of Meteorological Satellites (EUMETSAT) for providing freely available surface albedo data on their website.

Conflicts of Interest: The authors declare no conflict of interest.

References

1. Morocco Submits Enhanced NDC, Raising Ambition to 45.5 Percent by 2030, NDC Partnership. n.d. 2021. Available online: <https://ndcpartnership.org/news/morocco-submits-enhanced-ndc-raising-ambition-455-percent-2030> (accessed on 18 April 2021).

2. Green, M.A.; Keevers, M.J.; Thomas, I.; Lasich, J.B.; Emery, K.; King, R.R. 40% efficient sunlight to electricity conversion. *Prog. Photovolt. Res. Appl.* **2015**, *23*, 685–691. [[CrossRef](#)]
3. Lan, D.; Green, M.A. Pathways towards a 50% efficiency spectrum-splitting photovoltaic system: Application of built-in filters and generalization of concept. *Energy Procedia* **2018**, *150*, 83–86. [[CrossRef](#)]
4. Gueymard, C.A. Clear-sky irradiance predictions for solar resource mapping and large-scale applications: Improved validation methodology and detailed performance analysis of 18 broadband radiative models. *Sol. Energy* **2012**, *86*, 2145–2169. [[CrossRef](#)]
5. Pérez-Burgos, A.; Díez-Mediavilla, M.; Alonso-Tristán, C.; Rodríguez-Amigo, M.C. Analysis of solar direct irradiance models under clear-skies: Evaluation of the improvements for locally adapted models. *J. Renew. Sustain. Energy* **2017**, *9*, 023703. [[CrossRef](#)]
6. Popov, Z.; Nagy, Z.; Baranka, G.; Weidinger, T. Assessments of Solar, Thermal and Net Irradiance from Simple Solar Geometry and Routine Meteorological Measurements in the Pannonian Basin. *Atmosphere* **2021**, *12*, 935. [[CrossRef](#)]
7. Ineichen, P. Validation of models that estimate the clear sky global and beam solar irradiance. *Sol. Energy* **2016**, *132*, 332–344. [[CrossRef](#)]
8. Hunt, L.A.; Kuchar, L.; Swanton, C.J. Estimation of solar radiation for use in crop modelling. *Agric. For. Meteorol.* **1998**, *91*, 293–300. [[CrossRef](#)]
9. Badescu, V.; Gueymard, C.A.; Cheval, S.; Oprea, C.; Baci, M.; Dumitrescu, A.; Iacobescu, F.; Milos, I.; Rada, C. Computing global and diffuse solar hourly irradiation on clear sky. Review and testing of 54 models. *Renew. Sustain. Energy Rev.* **2012**, *16*, 1636–1656. [[CrossRef](#)]
10. Denhard, A.; Bandyopadhyay, S.; Habte, A.; Sengupta, M. *Evaluation of Time-Series Gap-Filling Methods for Solar Irradiance Applications*; National Renewable Energy Lab (NREL): Golden, CO USA, 2021; p. 33. [[CrossRef](#)]
11. El Alani, O.; Ghennioui, H.; Ghennioui, A.; Dahr, F.-E. Detection of clear sky instants from high frequencies pyranometric measurements of global horizontal irradiance. *E3S Web Conf.* **2021**, *229*, 1008. [[CrossRef](#)]
12. Pattarapanitchai, S.; Janjai, S. A semi-empirical model for estimating diffuse solar irradiance under a clear sky condition for a tropical environment. *Procedia Eng.* **2012**, *32*, 421–426. [[CrossRef](#)]
13. Bird, R.E.; Riordan, C. Simple Solar Spectral Model for Direct and Diffuse Irradiance on Horizontal and Tilted Planes at the Earth's Surface for Cloudless Atmospheres. *J. Appl. Meteorol. Climatol.* **1986**, *25*, 87–97. [[CrossRef](#)]
14. Iqbal, T.; Kundu, A. A Method for Determining the Solar Global and Defining the Diffuse and Beam Irradiation on a Clear Day. In *Modeling Solar Radiation at the Earth's Surface: Recent Advances*; Badescu, V., Ed.; Springer: Cham, Switzerland, 2008; pp. 93–113. [[CrossRef](#)]
15. Gueymard, C. REST2: High-performance solar radiation model for cloudless-sky irradiance, illuminance, and photosynthetically active radiation—Validation with a benchmark dataset. *Solar Energy* **2008**, *82*, 272–285. [[CrossRef](#)]
16. Hay, J.E. Satellite based estimates of solar irradiance at the earth's surface—I. Modelling approaches. *Renew. Energy* **1993**, *3*, 381–393. [[CrossRef](#)]
17. Nwokolo, S.C.; Ogbulezie, J.C. A qualitative review of empirical models for estimating diffuse solar radiation from experimental data in Africa. *Beni-Suef Univ. J. Basic Appl. Sci.* **2018**, *7*, 367–396. [[CrossRef](#)]
18. Bayrakçı, H.C.; Demircan, C.; Keçebas, A. The development of empirical models for estimating global solar radiation on horizontal surface—A case study. *Renew. Sustain. Energy Rev.* **2018**, *81*, 2771–2782. [[CrossRef](#)]
19. Benkacali, S.; Haddadi, M.; Khellaf, A. Evaluation of direct solar irradiance from 18 broadband parametric models: Case of Algeria. *Renew. Energy* **2018**, *125*, 694–711. [[CrossRef](#)]
20. Lefèvre, M.; Oumbe, A.; Blanc, P.; Espinar, B.; Gschwind, B.; Qu, Z.; Wald, L.; Schroedter-Homscheidt, M.; Hoyer-Klick, C.; Arola, A.; et al. McClear: A new model estimating downwelling solar radiation at ground level in clear-sky conditions. *Atmos. Meas. Tech.* **2013**, *6*, 2403–2418. [[CrossRef](#)]
21. Antonanzas, J.; Urraca, R.; Martínez-de-Pison, F.J.; Antonanzas-Torres, F. Solar irradiance mapping with exogenous data from support vector regression machines estimations. *Energy Convers. Manag.* **2015**, *100*, 380–390. [[CrossRef](#)]
22. Ruiz-Arias, J.A.; Gueymard, C.A. Worldwide inter-comparison of clear-sky solar radiation models. *AIP Conf. Proc.* **2016**, *1850*, 140018. [[CrossRef](#)]
23. Noia, M.; Ratto, C.F.; Festa, R. Solar irradiance estimation from geostationary satellite data: I. Statistical models. *Sol. Energy* **1993**, *51*, 449–456. [[CrossRef](#)]
24. Beyer, H.G.; Costanzo, C.; Heinemann, D. Modifications of the heliosat procedure for irradiance estimates from satellite images. *Sol. Energy* **1996**, *56*, 207–212. [[CrossRef](#)]
25. Zarzalejo, L.F.; Polo, J.; Martín, L.; Ramírez, L.; Espinar, B. A new statistical approach for deriving global solar radiation from satellite images. *Sol. Energy* **2009**, *83*, 480–484. [[CrossRef](#)]
26. Cano, D.; Monget, J.M.; Albuissou, M.; Guillard, H.; Regas, N.; Wald, L. A method for the determination of the global solar radiation from meteorological satellite data. *Sol. Energy* **1986**, *37*, 31–39. [[CrossRef](#)]
27. Polo, J.; Antonanzas-Torres, F.; Vindel, J.M.; Ramírez, L. Sensitivity of satellite-based methods for deriving solar radiation to different choice of aerosol input and models. *Renew. Energy* **2014**, *68*, 785–792. [[CrossRef](#)]
28. Daryl, R.M. Solar radiation modeling and measurements for renewable energy applications: Data and model quality. *Energy* **2005**, *30*, 1517–1531. [[CrossRef](#)]

29. Müller, R.; Dagestad, K.-F.; Ineichen, P.; Schroedter-Homscheidt, M.; Cros, S.; Dumortier, D.; Kuhlemann, R.; Olseth, J.; Izquierdo, G.; Reise, C.; et al. Rethinking satellite-based solar irradiance modelling The SOLIS clear-sky module. *Remote Sens. Environ.* **2004**, *91*, 160–174. [CrossRef]
30. Ineichen, P. A broadband simplified version of the Solis clear sky model. *Sol. Energy* **2008**, *82*, 758–762. [CrossRef]
31. Ineichen, P.; Perez, R. A new airmass independent formulation for the Linke turbidity coefficient. *Sol. Energy* **2002**, *73*, 151–157. [CrossRef]
32. Perez, R.; Ineichen, P.; Moore, K.; Kmiecik, M.; Chain, C.; George, R.; Vignola, F. A new operational model for satellite-derived irradiances: Description and validation. *Sol. Energy* **2002**, *73*, 307–317. [CrossRef]
33. Berger, X. Chauffage solaire et stratégies de chauffage. *Rev. Phys. Appl.* **1981**, *16*, 225–235. [CrossRef]
34. Adnot, J.; Bourges, B.; Campana, D.; Gicquel, R. Utilisation de Courbes de Fréquences Cumulées d'Irradiation Solaire Globale pour le Calcul des Installations Solaires. In *Analyse Statistique des Processus Météorologiques Appliquée à l'Énergie Solaire*; Lestienne, R., Ed.; CNRS: Strasbourg, France, 1979; pp. 9–40. Available online: <https://hal.archives-ouvertes.fr/hal-00993193> (accessed on 10 March 2022).
35. Haurwitz, B. Insolation in relation to cloudiness and cloud density. *J. Atmos. Sci.* **1945**, *2*, 154–166. [CrossRef]
36. Haurwitz, B. Insolation in relation to cloud type. *J. Atmos. Sci.* **1948**, *5*, 110–113. [CrossRef]
37. SOLCAST. 2022. Available online: <https://solcast.com/historical-and-tmy/> (accessed on 16 January 2022).
38. Gschwind, B.; Wald, L.; Blanc, P.; Lefèvre, M.; Schroedter-Homscheidt, M.; Arola, A. Improving the McClear model estimating the downwelling solar radiation at ground level in cloud free conditions—McClear-V3. *Meteorol. Z. Contrib. Atmos. Sci.* **2019**, *28*, 147–163. [CrossRef]
39. Mabasa, B.; Lysko, M.D.; Moloi, S.J. Validating Hourly Satellite Based and Reanalysis Based Global Horizontal Irradiance Datasets over South Africa. *Geomatics* **2021**, *1*, 429–449. [CrossRef]
40. Yang, D.; Bright, J.M. Worldwide validation of 8 satellite-derived and reanalysis solar radiation products: A preliminary evaluation and overall metrics for hourly data over 27 years. *Sol. Energy* **2020**, *210*, 3–19. [CrossRef]
41. Driemel, A.; Augustine, J.; Behrens, K.; Colle, S.; Cox, C.; Cuevas-Agulló, E.; Denn, F.M.; Duprat, T.; Fukuda, M.; Grobe, H.; et al. Baseline Surface Radiation Network BSRN: Structure and data description 1992–2017. *Earth Syst. Sci. Data* **2018**, *10*, 1491–1501. [CrossRef]
42. Bright, J. Solcast: Validation of a satellite-derived solar irradiance dataset. *Sol. Energy* **2019**, *189*, 435–449. [CrossRef]
43. Hersbach, H.; Bell, B.; Berrisford, P.; Hirahara, S.; Horányi, A.; Muñoz-Sabater, J.; Nicolas, J.; Peubey, C.; Radu, R.; Schepers, D.; et al. The ERA5 global reanalysis. *Q. J. R. Meteorol. Soc.* **2020**, *146*, 1999–2049. [CrossRef]
44. Lefèvre, M.; Wald, L. Validation of the McClear clear-sky model in desert conditions with three stations in Israel. *Adv. Sci. Res.* **2016**, *13*, 21–26. [CrossRef]
45. Mabasa, B.; Lysko, M.D.; Tazvinga, H.; Zwane, N.; Moloi, S.J. The Performance Assessment of Six Global Horizontal Irradiance Clear Sky Models in Six Climatological Regions in South Africa. *Energies* **2021**, *14*, 2583. [CrossRef]
46. Laaroussi, N.; El Azhary, K.; Garoum, M.; Raefat, S.; Feiz, A. Semi-empirical models for the estimation of global solar irradiance measurements in Morocco. In Proceedings of the 2016 3rd International Conference on Renewable Energies for Developing Countries REDEC, Zouk Mosbeh, Lebanon, 13–15 July 2016; pp. 1–6. [CrossRef]
47. Gairaa, K.; Benkacali, S.; Guermoui, M. Clear-sky models evaluation of two sites over Algeria for PV forecasting purpose. *Eur. Phys. J. Plus* **2019**, *134*, 534. [CrossRef]
48. Beyer, H.-G.; Czeplak, G.; Terzenbach, U.; Wald, L. Assessment of the method used to construct clearness index maps for the new European solar radiation atlas ESRA. *Sol. Energy* **1997**, *61*, 389–397. [CrossRef]
49. Rigollier, C.; Bauer, O.; Wald, L. On the clear sky model of the 4th European Solar Radiation Atlas with respect to the Heliosat method. *Sol. Energy* **2000**, *68*, 33–48. [CrossRef]
50. Xixi, S.; Bright, J.M.; Gueymard, C.A.; Acord, B.; Wang, P.; Engerer, N.A. Worldwide performance assessment of 75 global clear-sky irradiance models using Principal Component Analysis. *Renew. Sustain. Energy Rev.* **2019**, *111*, 550–570. [CrossRef]
51. Laguarda, A.; Abal, G. Clear-Sky Broadband Irradiance: First Model Assessment in Uruguay. In Proceedings of the SWC2017/SHC2017, IEA SHC Solar Heating and Cooling Conference 2017, Abu Dhabi, United Arab Emirates, 29 October–2 November 2017; pp. 1–12. [CrossRef]
52. Kasten, F.; Czeplak, G. Solar and terrestrial radiation dependant on the amount of type of cloud. *Sol. Energy* **1980**, *24*, 177–189. [CrossRef]
53. Kasten, F. Parametrisierung der Globalstrahlung durch Bedeckungsgrad und Trübungsfaktor. *Ann. Meteorol. Neue* **1983**, *20*, 49–50.
54. Reno, M.; Hansen, C.; Stein, J. *Global Horizontal Irradiance Clear Sky Models: Implementation and Analysis*; Sandia Report, SAND2012-2389; Sandia National Laboratories: Albuquerque, NM, USA, 2014; p. 69. [CrossRef]
55. Yang, D.; Jirutitijaroen, P.; Walsh, W.M. The estimation of clear sky global horizontal irradiance at the equator. *Energy Procedia* **2012**, *25*, 141–148. [CrossRef]
56. Gueymard, V.B.; Cheval, S.; Oprea, C.; Baciu, M.; Dumitrescu, A.; Iacobescu, F.; Milos, I.; Rada, C. Accuracy analysis for fifty-four clear-sky solar radiation models using routine hourly global irradiance measurements in Romania. *Renew. Energy* **2013**, *55*, 85–103. [CrossRef]

57. Badescu, V.; Gueymard, C.A.; Cheval, S.; Oprea, C.; Baciu, M.; Dumitrescu, A.; Iacobescu, F.; Milos, I.; Rada, C. Accuracy and sensitivity analysis for 54 models of computing hourly diffuse solar irradiation on clear sky. *Theor. Appl. Climatol.* **2013**, *111*, 379–399. [[CrossRef](#)]
58. Kwarikunda, N.; Chiguvare, Z. Performance Analysis of Clear Sky Global Horizontal Irradiance Models: Simple Models Adapted for Local Conditions. *J. Renew. Energy* **2021**, *2021*, 4369959. [[CrossRef](#)]
59. El Mghouchi, Y.; El Bouardi, A.; Sadouk, A.; Fellak, I.; Ajzoula, T. Comparison of three solar radiation models and their validation under all sky conditions—Case study: Tetuan city in northern of Morocco. *Renew. Sustain. Energy Rev.* **2016**, *58C*, 1432–1444. [[CrossRef](#)]
60. ASHRAE. *Handbook of Fundamentals*; American Society of Heating, Refrigeration, and Air-Conditioning Engineers: Atlanta, GA, USA, 1985.
61. Yao, W.; Xu, C.; Zhao, J.; Wang, X.; Wang, Y.; Li, X.; Cao, J. The modified ASHRAE model based on the mechanism of multi-parameter coupling. *Energy Convers. Manag.* **2021**, *209*, 112642. [[CrossRef](#)]
62. Campbell, G.S.; Norman, J.M. *An Introduction to Environmental Biophysics*, 2nd ed.; Springer: New York, NY, USA, 1988; 306p, ISBN 0-387-94937-2.
63. Bird, R.E. A simple, solar spectral model for direct normal and diffuse horizontal irradiance. *Sol. Energy* **1984**, *32*, 461–471. [[CrossRef](#)]
64. Liu, B.Y.H.; Jordan, R.C. The interrelationship and characteristic distribution of direct, diffuse, and total solar radiation. *Sol. Energy* **1960**, *4*, 1–19. [[CrossRef](#)]
65. Kallio, V.; Riihelä, A. Comparative Validation of Clear Sky Irradiance Models over Finland. In Proceedings of the IGARSS 2018—2018 IEEE International Geoscience and Remote Sensing Symposium, Valencia, Spain, 22–27 July 2018; pp. 1199–1202. [[CrossRef](#)]
66. Holmgren, W.F.; Hansen, C.W.; Mikofski, M.A. pvlib python: A python package for modeling solar energy systems. *J. Open Source Softw.* **2018**, *3*, 884. [[CrossRef](#)]
67. Alam, S. Prediction of direct and global solar irradiance using broadband models: Validation of REST model. *Renew. Energy* **2006**, *31*, 1253–1263. [[CrossRef](#)]
68. Gueymard, C.A. Critical analysis and performance assessment of clear sky solar irradiance models using theoretical and measured data. *Sol. Energy* **1993**, *51*, 121–138. [[CrossRef](#)]
69. Ineichen, P. Comparison of eight clear sky broadband models against 16 independent data banks. *Sol. Energy* **2006**, *80*, 468–478. [[CrossRef](#)]
70. Younes, S.; Muneer, T. Clear-sky classification procedures and models using a world-wide data-base. *Appl. Energy* **2007**, *84*, 623–645. [[CrossRef](#)]
71. Gueymard, C. Progress in direct irradiance modeling and validation. In Proceedings of the Solar 2010 Conference, American Solar Energy Society, Phoenix, AZ, USA, 17–22 May 2010; Available online: https://www.solarconsultingservices.com/public/Gueymard-DNI_models_validation-ASES10.pdf (accessed on 12 May 2022).
72. Ianetz, A.; Lyubansky, V.; Setter, I.; Kriheli, B.; Evseev, E.G.; Kudish, A.I. Inter-comparison of different models for estimating clear sky solar global radiation for the Negev region of Israel. *Energy Convers. Manag.* **2007**, *48*, 259–268. [[CrossRef](#)]
73. Iqbal, M. *An Introduction to Solar Radiation*, 1st ed.; Elsevier: Amsterdam, The Netherlands, 1983; ISBN 9780323151818.
74. Lingamgunta, C.; Veziroglu, T.N. A universal relationship for estimating clear sky insolation. *Energy Convers. Manag.* **2004**, *45*, 27–52. [[CrossRef](#)]
75. Kondratyev, K.Y. *Radiation in the Atmosphere*, 1st ed.; Elsevier: Amsterdam, The Netherlands, 1969; Volume 12, ISBN 9780080954479.
76. Holtslag, A.A.M.; Van Ulden, A.P. A Simple Scheme for Daytime Estimates of the Surface Fluxes from Routine Weather Data. *J. Appl. Meteorol.* **1983**, *22*, 517–529. [[CrossRef](#)]
77. Bálint, R.; Fodor, A.; Szalkai, I.; Szalkai, Z.; Magyar, A. Modeling and calculatuionn of the global solar irradiance on slopes. *Hung. J. Ind. Chem.* **2019**, *47*, 57–63. [[CrossRef](#)]
78. Brimicombe, C.; Quintino, T.; Smart, S.; Di Napoli, C.; Hogan, R.; Cloke, H.L.; Pappenberger, F. *Calculating the Cosine of the Solar Zenith Angle for Thermal Comfort Indices*; ECMWF Technical Memorandum No. 895; European Centre for Medium-Range Weather Forecasts: Reading, UK, 2022; 18p.
79. Available online: <https://climateknowledgeportal.worldbank.org/country/morocco/climate-data-historical> (accessed on 26 October 2021).
80. Allouhi, A.; Kousksou, T.; Jamil, A.; El Rhafiki, T.; Mourad, Y.; Zeraouli, Y. Economic and environmental assessment of solar air-conditioning systems in Morocco. *Renew. Sustain. Energy Rev.* **2015**, *50*, 770–781. [[CrossRef](#)]
81. Allouhi, A.; Jamil, A.; Kousksou, T.; El Rhafiki, T.; Mourad, Y.; Zeraouli, Y. Solar domestic heating water systems in Morocco: An energy analysis. *Energy Convers. Manag.* **2015**, *92*, 105–113. [[CrossRef](#)]
82. Meteomanz. Available online: <http://www.meteomanz.com/index?l=1> (accessed on 16 January 2022).
83. Zahumenský, I. *Guidelines on Quality Control Procedures for Data from Automatic Weather Stations*; World Meteorological Organization: Geneva, Switzerland, 2004; pp. 1–10.
84. Born, K.; Fink, A.; Paeth, H. Dry and wet periods in the northwestern Maghreb for present day and future climate conditions. *Meteorol. Z.* **2008**, *17*, 533–551. [[CrossRef](#)]

85. Filahi, S.; Tanarhte, M.; Mouhir, L.; El Morhit, M.; Trambly, Y. Trends in indices of daily temperature and precipitations extremes in Morocco. *Theor. Appl. Climatol.* **2016**, *124*, 959–972. [CrossRef]
86. Hong, C.; Qin, W.; Wang, L.; Hu, B.; Zhang, M. Hourly clear-sky solar irradiance estimation in China: Model review and validations. *Sol. Energy* **2021**, *226*, 468–482. [CrossRef]
87. Keogh, W.M.; Blakers, A.W. Accurate measurement, using natural sunlight, of silicon solar cells. *Prog. Photovolt.* **2004**, *12*, 1–19. [CrossRef]
88. Gueymard, C. Analysis of monthly average atmospheric precipitable water and turbidity in Canada and northern United States. *Sol. Energy* **1994**, *53*, 57–71. [CrossRef]
89. Gueymard, C. Assessment of the Accuracy and Computing Speed of Simplified Saturation Vapor Equations Using a New Reference Dataset. *J. Appl. Meteorol.* **1993**, *32*, 1294–1300. [CrossRef]
90. Schroedter-Homscheidt, M.; Arola, A.; Killius, N.; Lefèvre, M.; Saboret, L.; Wandji, W.; Wey, E. The Copernicus atmosphere monitoring service CAMS radiation service in a nutshell. In Proceedings of the Sixteenth European Photovoltaic Solar Energy Conference, SolarPACES16, Glasgow, UK, 1–5 May 2016; pp. 11–14. Available online: <https://hal-mines-paristech.archives-ouvertes.fr/hal-01386187> (accessed on 12 January 2021).
91. SODA Portal. Available online: <http://www.soda-pro.com/web-services/atmosphere/linke-turbidity-factor-ozone-water-vapor-and-angstrom> (accessed on 21 November 2021).
92. SODA Portal. Available online: <http://www.soda-pro.com/web-services/atmosphere/cams-aod> (accessed on 26 October 2021).
93. Ångström, A. On the Atmospheric Transmission of Sun Radiation and on Dust in the Air. *Geogr. Ann.* **1929**, *11*, 156–166. [CrossRef]
94. Ångström, A. Techniques of Determining the Turbidity of the Atmosphere. *Tellus* **1961**, *13*, 214–223. [CrossRef]
95. Karlsson, K.-G.; Anttila, K.; Trentmann, J.; Stengel, M.; Fokke Meirink, J.; Devasthale, A.; Hanschmann, T.; Kothe, S.; Jääskeläinen, E.; Sedlar, J.; et al. CLARA-A2: The second edition of the CM SAF cloud and radiation data record from 34 years of global AVHRR data. *Atmos. Chem. Phys.* **2017**, *17*, 5809–5828. [CrossRef]
96. Reda, I.; Andreas, A. Solar position algorithm for solar radiation applications. *Sol. Energy* **2004**, *76*, 577–589. [CrossRef]
97. Duffie, J.A.; Beckman, W.A. *Solar Engineering of Thermal Processes*; John Wiley & Sons, Inc.: Hoboken, NJ, USA, 1980; pp. 6–13, 22.
98. Cooper, P.I. The absorption of radiation in solar stills. *Sol. Energy* **1969**, *12*, 333–346. [CrossRef]
99. Spencer, J.W. Fourier series representation of the position of the sun. *Search* **1971**, *2*, 172.
100. Kasten, F.; Young, A.T. Revised optical air mass tables and approximation formula. *Appl. Opt.* **1989**, *28*, 4735–4738. [CrossRef]
101. Bird, R.E.; Hulstrom, R.L. *Simplified Clear Sky Model for Direct and Diffuse Insolation on Horizontal Surfaces*; No. SERI/TR-642-761; Solar Energy Research Institute: Golden, CO, USA, 1981.
102. Gueymard, C.A. The sun's total and spectral irradiance for solar energy applications and solar radiation models. *Sol. Energy* **2004**, *76*, 423–453. [CrossRef]
103. Engerer, N.A.; Mills, F.P. Validating nine clear sky radiation models in Australia. *Sol. Energy* **2015**, *120*, 9–24. [CrossRef]
104. Javu, L.; Winkler, H.; Roro, K. Validating clear-sky irradiance models in five South African locations. In Proceedings of the Southern African Solar Energy Conference 2019 SASEC2019, Mpekwani, Eastern Cape, South Africa, 25–27 November 2019; Available online: <http://hdl.handle.net/10204/11889> (accessed on 15 February 2022).
105. Farahat, A.; Kambezidis, H.D.; Almazroui, M.; Ramadan, E. Solar Potential in Saudi Arabia for Southward-Inclined Flat-Plate Surfaces. *Appl. Sci.* **2021**, *11*, 4101. [CrossRef]

Disclaimer/Publisher's Note: The statements, opinions and data contained in all publications are solely those of the individual author(s) and contributor(s) and not of MDPI and/or the editor(s). MDPI and/or the editor(s) disclaim responsibility for any injury to people or property resulting from any ideas, methods, instructions or products referred to in the content.